
Interaction Between HII Region and AFGL 333-Ridge: Implications to the Star Formation Scenario

Makoto NAKANO^{1,*}, Takashi SOEJIMA¹, James O. CHIBUEZE² Takumi
NAGAYAMA³, Toshihiro OMODAKA⁴, Toshihiro HANDA⁴, Kazuyoshi
SUNADA³, Tatsuya KAMEZAKI⁴, Ross A. BURNS^{4,5}

¹Faculty of Education, Oita University, 700 Dannoharu, Oita 870-1192, Japan.

²Department of Physics and Astronomy, Faculty of Physical Sciences,
University of Nigeria, Carver Building, 1 University Road, Nsukka, Nigeria.

³Mizusawa VLBI Observatory, National Astronomical Observatory of Japan, 2-21-1 Osawa,
Mitaka, Tokyo 181-8588, Japan.

⁴Department of Physics and Astronomy, Graduate School of Science and Engineering,
Kagoshima University, 1-21-35 Korimoto, Kagoshima 890-0065, Japan.

⁵Joint Institute for VLBI ERIC (JIVE), Postbus 2, 7990 AA Dwingeloo, the Netherlands

*E-mail: mnakano@oita-u.ac.jp

Received 2016 July 7; Accepted 2016 November 18

Abstract

We investigated the star formation activities in the AFGL 333 region, which is in the vicinity of the W4 expanding bubble, by conducting NH_3 (1,1), (2,2), and (3,3) mapping observations with the 45 m Nobeyama Radio Telescope at an angular resolution of $75''$. The morphology of the NH_3 (1,1) map shows a bow-shape structure with the size of 2.0×0.6 pc as seen in the dust continuum. At the interface between the W4 bubble and the dense NH_3 cloud, the compact HII region G 134.2+0.8, associated with IRAS 02245+6115, is located. Interestingly, just north and south of G 134.2+0.8 we found NH_3 emission exhibiting large velocity widths of ~ 2.8 km s⁻¹, compared to 1.8 km s⁻¹ at the other positions. As the possibility of mechanical energy injection through the activity of YSO(s) is low, we considered the origin of the large

turbulent gas motion as indication of interaction between the compact HII region and the periphery of the dense molecular cloud. We also found expanding motion of the CO emission associated with G 134.2+0.8. The overall structure of the AFGL 333-Ridge might have been formed by the expanding bubble of W4. However, the small velocity widths observed west of IRAS 02245+6115, around the center of the dense molecular cloud, suggest that interaction with the compact HII region is limited. Therefore the YSOs (dominantly Class 0/I) in the core of the AFGL 333-Ridge dense molecular cloud most likely formed in quiescent mode. As has been previously suggested for the large scale star formation in the W3 giant molecular cloud, our results show an apparent coexistence of induced and quiescent star formation in this region. It appears that star formation in the AFGL 333 region has proceeded without significant external triggers, but accompanying stellar feedback environment.

Key words: stars: formation – ISM: clouds – ISM: individual objects (AFGL 333) – HII regions

1 Introduction

The influence of HII regions on their immediate surrounding, especially in inducing star formation activities, has drawn a lot of attentions in recent times. Elmegreen & Lada (1977) first proposed that high-mass stars are formed through a “collect-and-collapse” sequential process triggered by the influence of an expanding HII region. Later, Whitworth et al. (1994) explained why gravitationally unstable fragments are formed in the shocked layers which fragment to produce high-mass stars. Since then many observational studies have targeted triggered star formation (e.g. Carpenter et al. 2000; Lefloch & Cernicharo 2000; Deharveng et al. 2005). Although examples of quiescent formation of low mass stars have been reported in regions such as Taurus, those for high mass stars are rare, KR 140 (Ballantyne et al. 2000) being one example. While the influence of expanding HII regions on their surroundings cannot be denied, Chibueze et al. (2013) argued an isolated case of the star associated with S 252A forming spontaneously though located near the shock fronts of the Monkey Head Nebula (Gem OB1). Identifying the formation scenario requires studying the cloud properties and star formation in regions under the influence of HII regions.

W3 Main, W3(OH) and AFGL 333 are active massive star forming regions located in the high-density layer (HDL) on the western edge of the W4 expanding HII region, or bubble (Lada et al. 1978). W4 is excited by a group of O stars located at the central part of the HII region (Lefloch et al. 1997). Oey et al. (2005) suggested a three generation system of hierarchical triggered star formation,

based on the stellar populations of IC 1795. The first generation is the 1300 pc loop and the Perseus superbubble. These triggered the formation of IC 1795, and then IC 1795 triggered the formation of W3 North, W3 Main, W3 OH at the edge of shell. An X-ray study by Feigelson & Townsley (2008) revealed the diversity of the W3 stellar populations. Roccatagliata et al. (2011) analyzed the protoplanetary disks of young stars in the IC 1795 region as massive star forming region by a deep Spitzer survey. The wider area including AFGL 333 and KR 140 has been investigated with Spitzer and Herschel (Rivera-Ingraham et al. 2011, 2013). Observational results of a sub-mm survey of dense clumps by Moore et al. (2007), and extensive molecular line observations by Polychroni et al. (2012) agree well with the collect-and-collapse model. Bieging & Peters (2011) also produced the extensive CO maps of the W3 region. Star formation in W3 Main and W3 (OH) are considered to have been triggered by IC 1795. On the other hand KR 140, which is located in the southwest quadrant of W3 giant molecular cloud (GMC), appears to be formed in quiescently. Recently much of works have been done to reveal the star formation history of the W3 complex. The stellar contents in W3 Main (Bik et al. 2014), IC 1795 (Román-Zúñiga et al. 2015), and across the complex (Kiminki et al. 2015) were investigated. The statistical study was done by using Herschel datasets (Rivera-Ingraham et al. 2015). These studies showed a complex history of star formation in the W3 GMC, and suggested massive stars and clusters in the active region as W3 Main and W3 (OH) were formed in the dense material by the progression of star formation process. Although triggering events play an important role to form the active region, it is still unclear in more quiescent region as AFGL 333 or KR 140. AFGL 333-Ridge is a dense molecular cloud located south of W3(OH). It is associated with three known IRAS sources, namely, IRAS 02252+6120 (SFO 05: Sugitani et al. 1991), IRAS 02244+6117, and IRAS 02245+6115 (AFGL 333) (See figure 1). Although AFGL 333 is located in the HDL, its star formation is less active than the other two regions (W3 Main and W3 (OH)) and it has less extreme environmental conditions (e.g. Rivera-Ingraham et al. 2013). The deep NIR photometry by Jose et al. (2016) unraveled the star formation activity of AFGL 333 region. The AFGL 333 region is one of the best sites to study the influence of HII regions to star formation because of its location; the dense molecular cloud at the edge of the extended bubble (Heart Nebula) of W4 and the presence of a compact HII region in IRAS 02245+6115.

To study the interaction between HII regions and molecular clouds, investigation of the distribution of dense gas and of the gas temperature is vital. NH_3 lines prove to be particularly useful for investigating the physical conditions of dense gas clumps of a molecular cloud. The NH_3 observations have advantages compared to other lines, such as ^{13}CO and C^{18}O , because NH_3 is an intermediate-density gas tracer, and gives gas temperature using the $(2, 2)/(1, 1)$ line ratio. The information on gas motion and temperature distribution can indicate signs of interaction. It also reveals the presence

of interstellar shocks through the (3,3)/(1,1) line ratio, shown by Nagayama et al. (2009). As example of such a study is given in Urquhart et al. (2011) who surveyed massive young stellar objects and ultra-compact HII regions in ammonia – allowing them to derive the basic physical properties of the associated high density gas for their sample. As such, we made mapping observations of the AFGL 333 region using NH₃ (1,1), (2,2), and (3,3) lines and estimated the distribution of the gas kinetic temperature over the cloud. We also simultaneously observed H₂O maser emission which is a well known tracer of early star formation activity (e.g. Sunada et al. 2007).

In this paper, we observationally investigate the dense clumps of the molecular cloud in the AFGL 333 region that are influenced by the expanding HII region, and compared our results with archival data/catalogs to reveal the local star formation scenario in this region. The parallax distance of W3(OH) was obtained to be 2.0 kpc (Xu et al. 2006; Hachisuka et al. 2006). Since the line of sight velocities of W4 and W3(OH) are within of 5 km s⁻¹ of each other, we will assume a common distance of 2.0 kpc for the AFGL 333 region in this paper.

2 Observations

2.1 NH₃ and H₂O Maser Observations

We conducted NH₃ and H₂O maser observations of the AFGL 333 region using the 45 m telescope at Nobeyama Radio Observatory (NRO) between January and June 2013. NH₃ (J,K) = (1,1), (2,2), and (3,3) lines, whose frequencies are 23.694495 GHz, 23.722633 GHz, and 23.870129 GHz, respectively, and the 22.235080 GHz H₂O maser line were observed simultaneously. We used the H22 receiver, a cooled HEMT receiver, and the SAM45, a digital spectrometer, with eight IFs to observe both polarizations for each line simultaneously. The bandwidth and spectral resolution of each IF were 62 MHz and 30.5 kHz, respectively corresponding to ~ 800 km s⁻¹ and ~ 0.39 km s⁻¹ for the observed lines. The telescope beam size at 23 GHz is 75'', which corresponds to 0.73 pc at 2.0 kpc. We observed 267 positions with a 37.5'' grid along the Galactic coordinates using position switching between the target and the reference position comprising of the empty sky. We investigated the kinematic and density structure of the AFGL 333 region at clump scales, or 0.5-1.0 pc. The reference position was taken at $(l, b) = (134^\circ 3400, 0^\circ 5500)$, where no NH₃ or H₂O maser was detected. The target mapping area of the AFGL 333 region was 600'' \times 1000'' centered at $(l, b) = (134^\circ 2000, 0^\circ 7500)$. Figure 1 shows the mapping area of the l - b observations overlaid on the Spitzer-IRAC image. The pointing accuracy was checked using an H₂O maser source Cepheus A and was better than 5''.

Data reduction was carried out using the NEWSTAR software package developed by the Nobeyama Radio Observatory (NRO). Emission free channels were used to estimate and subtract

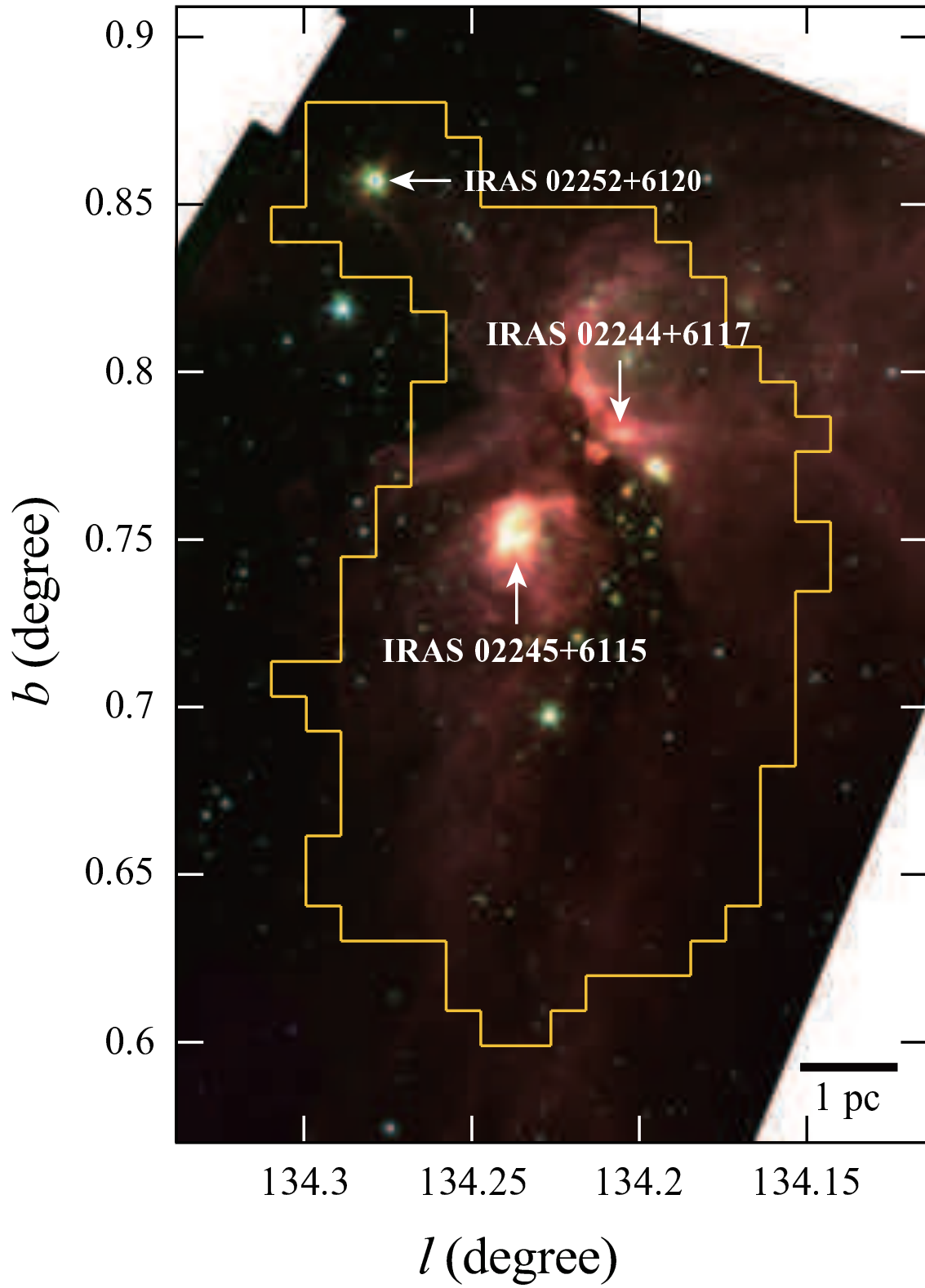


Fig. 1. Three-color (red: $8.0 \mu\text{m}$, green: $5.8 \mu\text{m}$, blue: $4.5 \mu\text{m}$) Spitzer-IRAC image of the AFGL 333 region. Yellow enclosure shows the mapping area of our NH_3 observations.

a spectral baseline. We applied only the linear line as the continuum level. Vertical and horizontal polarizations were combined and weighted based on the system noise temperature which was between 100 and 300 K. The antenna temperature in Kelvin scale was measured using the chopper wheel method (Kutner & Ulich 1981). The median 1σ rms noise level was 0.04 K. For the H₂O maser data. We converted the antenna temperature to the flux density using the conversion factor of 2.6 Jy K^{-1} . In this paper, the intensities of NH₃ and H₂O maser are presented as the antenna temperature in Kelvin and flux density in Jansky, respectively.

2.2 Archival Data/Catalog

We used the data cubes of the J=2-1 lines of ¹²CO and ¹³CO obtained by the Heinrich Hertz Submillimeter Telescope (Bieging & Peters 2011). The effective resolution of the maps is $38''$ FWHM and the sampling velocity of 0.5 km s^{-1} . 1420 MHz radio continuum data from the Canadian Galactic Plane Survey (CGPS: Taylor et al. 2003) was also used to analyse the ionized gas distribution. The image was obtained with a synthesized beam and an rms noise of $1.0 \times 0.81 \text{ arcmin}^2$ and 0.063 K.

To establish the distributions of young stars and dust, we obtained Spitzer Space Telescope 3.6, 4.5, 5.8 and 8.0 μm IRAC image of the AFGL 333 region from the Spitzer Heritage Archive hosted by the Infrared Science Archive at IPAC (Post-Basic Calibrated Data: Program ID 30995), which shows the bright IRAS sources (clusters) and a prominent infrared dark filament representing the AFGL 333-Ridge dense molecular cloud. We also used the Spitzer YSO catalog in this region (Catalog 1 by Rivera-Ingraham et al. (2011)), and the photometric data of all point sources within AFGL 333 by Jose et al. (2016).

3 Results

3.1 Spatial Distribution of NH₃

NH₃ (J, K) = (1,1), (2,2), and (3,3) emission for which the integrated intensities exceed the 2σ noise level ($\geq 0.14 \text{ K km s}^{-1}$), were obtained at 165, 111, and 71 positions out of the 267 observed positions, respectively. Figure 2 shows the NH₃ (1,1), (2,2), and (3,3) profiles towards the (1,1) emission peak at $(l, b) = (134.^{\circ}2104, 0.^{\circ}7188)$. The NH₃ line profile comprises five quadruple hyperfine components consisting of a main line and two symmetrical pairs of inner and outer satellite lines. We could detect the inner and outer satellite lines of the (1,1) line in 51 positions. These 51 positions show (2,2) main lines with $> 2\sigma$, and 36 points show (3,3) main lines among them. Detections of both main and satellite lines in (1,1) lines yield an opacity estimation using their intensity ratio (see subsection 3.3). The satellite lines of (2,2) and (3,3) line were not detected at any positions in the observed area.

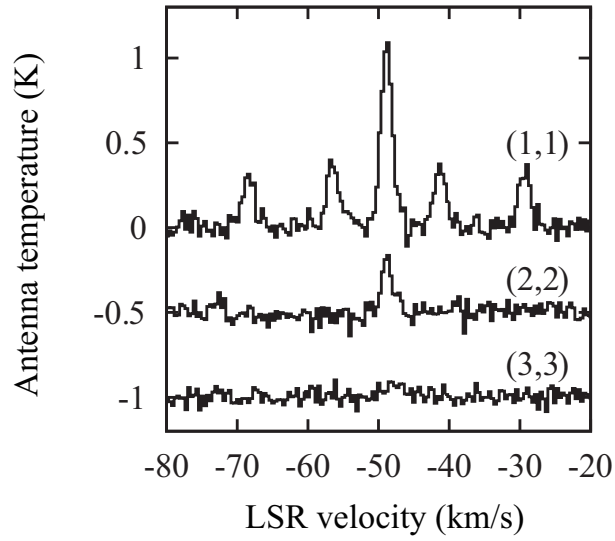


Fig. 2. NH_3 (1,1), (2,2) and (3,3) spectra towards the (1,1) emission peak at $(l, b) = (134^\circ 2104, 0^\circ 7188)$, shown in figure 3.

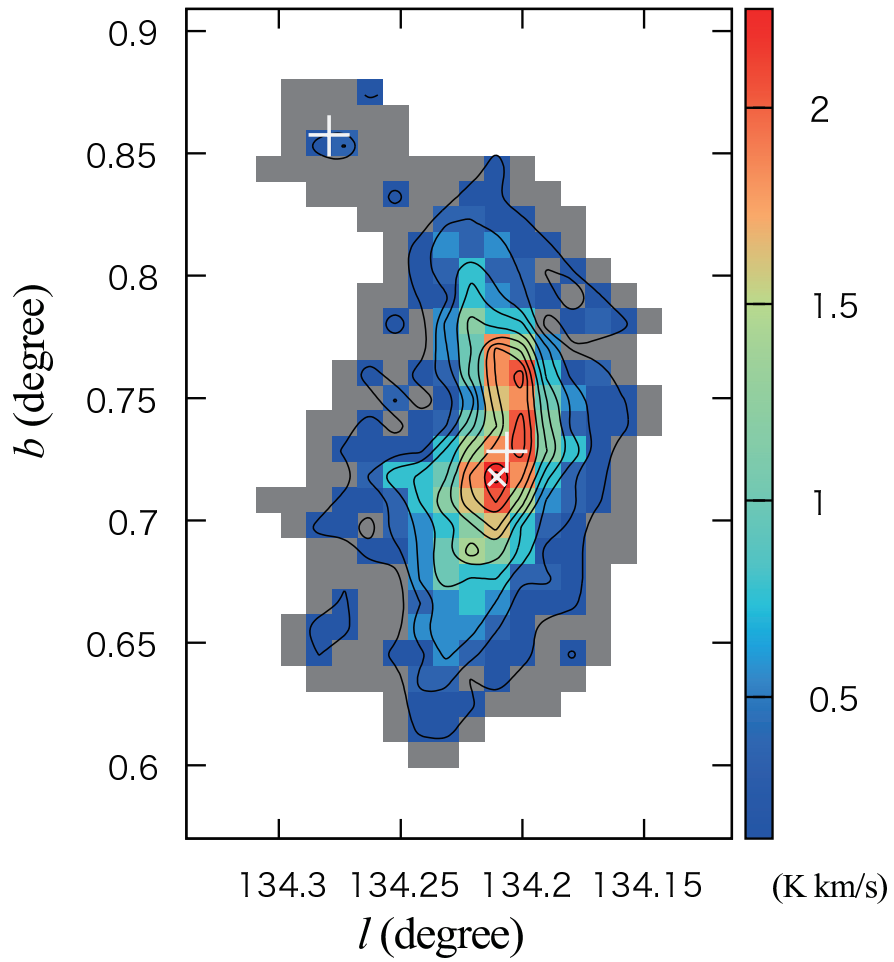


Fig. 3. Integrated intensity map of NH_3 (1,1) line. The lowest contour and contour interval are 0.14 K km s^{-1} (2σ) and 0.22 K km s^{-1} respectively. The integrated velocity range is from -52.0 to -45.5 km s^{-1} . Pluses and cross denote the positions of two H_2O masers, and the (1,1) emission peak, respectively.

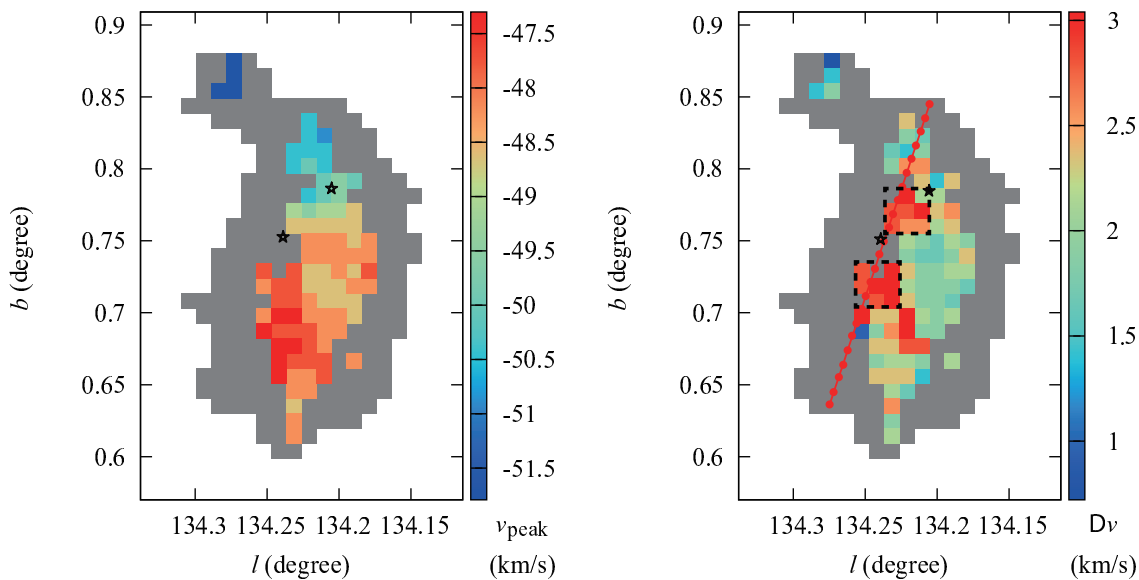


Fig. 4. Peak velocity (left) and velocity width (right) maps of NH_3 (1,1) line. The region of large velocity width is shown by the dashed boxes. Stars indicate the positions of IRAS 02245+6115 and IRAS 02244+6117.

Figure 3 shows the l - b map of (1,1) line, velocity-integrated in the range from $v_{\text{LSR}} = -52.0$ to -45.5 km s^{-1} . No significant (1,1) emission was detected beyond this velocity range. (1,1) emission is distributed with an area of $\Delta l \times \Delta b \simeq 0^\circ.15 \times 0^\circ.25$ ($5.2 \times 8.7 \text{ pc}$ at the distance of 2.0 kpc). The overall morphology shows bow shape with the size of $3'.4 \times 1'.0$ ($2.0 \times 0.6 \text{ pc}$) at the level of half of peak intensity. There is weak and compact emission at north-east of the ridge near $(l, b) \simeq (134^\circ.27, 0^\circ.86)$ corresponding to the position of SFO 05 (Fukuda et al. 2013) at the northern tip of the infrared dark filament. SFO 05 is a small bright-rimmed cloud with an optical size of $< 1'$. This bright-rimmed cloud was observed with the Green Bank telescope in NH_3 (1,1) and (2,2) lines (Morgan et al. 2010). The bow-shaped distribution of the (1,1) line is similar to those of the ^{13}CO and C^{18}O (Sakai et al. 2006), submillimeter observations (Di Francesco et al. 2008), Herschel far infrared map (Rivera-Ingraham et al. 2013), and the filamentary structure of the dark infrared cloud (Rivera-Ingraham et al. 2011).

3.2 Velocity Distribution of NH_3

Figure 4 shows the peak velocity and velocity width maps of (1,1) line. The peak velocity and the velocity width were obtained from the Gaussian fitting to the main line of the (1,1) spectrum. We observe a north-south velocity gradient along the ridge from the peak velocity map. The most blueshifted component of $v_{\text{LSR}} = -51.5 \text{ km s}^{-1}$ is detected near the position of SFO 05. This velocity is consistent with that of Morgan et al. (2010). SFO 05 should be on the near side of W4. Bieging & Peters (2011)

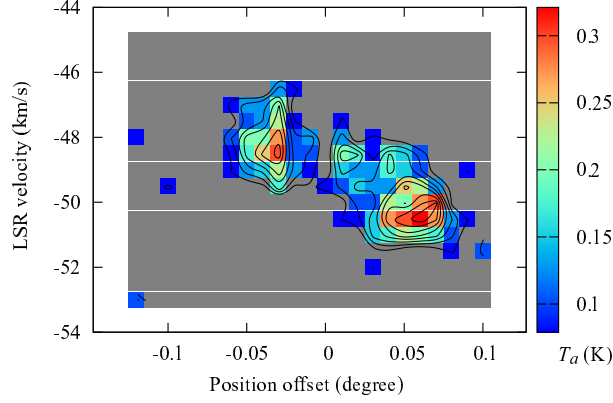


Fig. 5. Position velocity map of NH_3 (1,1) line. The lowest contour and contour interval are 0.08 K (2σ) and 0.03 K, respectively. The position offset, increasing toward the northwest, is relative to the position of IRAS 02245+6115 along the line shown in figure 4.

reported that the AFGL 333 region shows the most negative velocity emission in the high density layer (HDL). The velocity structure in the AFGL 333 region is also consistent with the C^{18}O results by Sakai et al. (2007), blueshifted at the northside of the NH_3 peak, and redshifted at the southern side. This may indicate that the gas is kinematically distributed by the large scale motion (> 10 pc) of HDL. AFGL 333 is located on the near side of the W4 bubble, and W3 Main and W3 (OH) are at the edge or far side of the bubble, as suggested by Thronson et al. (1985). The inverse trend of the velocity structure near the center may reflect the small scale structure within the clumps.

We found two regions of large velocity width at the eastern side of the ridge, one north and the other south of the dent. The (1,1) emission velocity widths of these two regions are $2.8 \pm 0.4 \text{ km s}^{-1}$, compared to $1.8 \pm 0.1 \text{ km s}^{-1}$ at the other positions. Jose et al. (2016) reported YSO surface density peaks at the center of the cluster associated with IRAS 02245+6115. Figure 5 shows the position velocity diagram of the (1,1) emission line along the line in figure 4.

We made the ^{13}CO J=2-1 integrated intensity maps in two velocity intervals, which is shown in figure 6, by using the data cubes provided by Bieging & Peters (2011). The blue shifted components (-50.0 km s^{-1}) mainly consist of the curved ridge at the east of IRAS 02244+6117, and two clumps at the west and the south of IRAS 02245+6115. The northern NH_3 large velocity width region corresponds to the part of this curved CO ridge. The red shifted components (-47.5 km s^{-1}) mainly consist of the circular ridge with the size of $0^{\circ}05$ around IRAS 02245+6115, and the southern extension. The southern NH_3 large velocity width region corresponds to the part of this circular CO ridge. AFGL 333-Ridge, we confirmed on the NH_3 maps, are not so conspicuous on the ^{13}CO maps. This may show the difference of the critical density of the molecular species. NH_3 emission sampled denser main part of the AFGL 333-Ridge.

We discuss the origin of these NH_3 large velocity width regions in subsection 4.2.

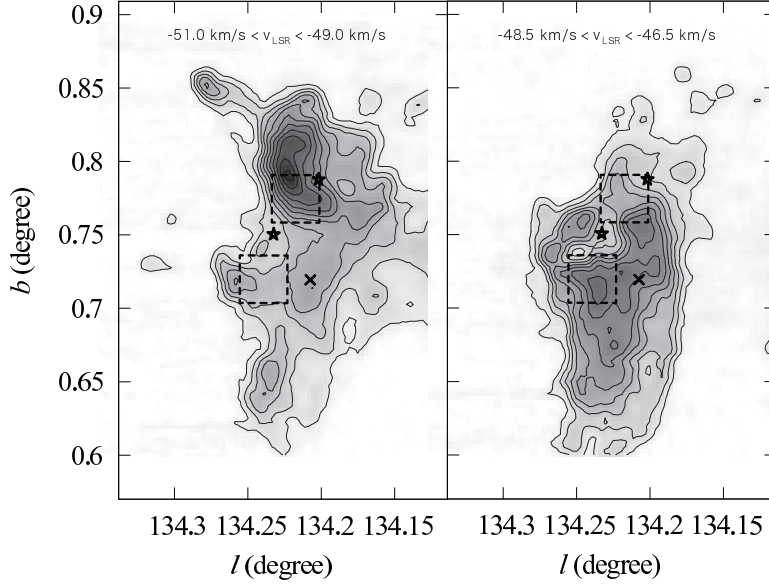


Fig. 6. ^{13}CO J=2-1 integrated intensity maps in two velocity intervals, (a) $-51.0 < v_{\text{LSR}} < -49.0 \text{ km s}^{-1}$, and (b) $-48.5 < v_{\text{LSR}} < -46.5 \text{ km s}^{-1}$, from the dataset of Bieging & Peters (2011). Two IRAS sources, large NH_3 line width regions, and an NH_3 peak position are shown in stars, boxes, and x, respectively. The lowest contour and contour interval are 2.5 K km s^{-1} (5σ) and 2.5 K km s^{-1} , respectively.

3.3 Physical Parameters

From the NH_3 observational results, we derived the physical parameters: optical depth, column density, rotational temperature, local thermodynamical equilibrium mass, and virial mass of AFGL 333-Ridge.

The optical depth of NH_3 can be derived from the intensity ratio between the main and satellite line using the method shown in Ho & Townes (1983). The theoretical intensity ratio of satellite to main lines is

$$\frac{T_a(\text{main})}{T_a(\text{sate})} = \frac{1 - e^{-\tau}}{1 - e^{-a\tau}} \quad (1)$$

In the case of the inner satellite line and outer satellite line, a is 0.278 and 0.222, respectively. Figure 7 shows the correlation between the NH_3 (1,1) and the inner/outer satellite lines. The correlation shows a fairly uniform intensity ratio for all observed positions. The ratios of the inner and outer satellite lines to main line were obtained to be 0.344 ± 0.015 and 0.267 ± 0.014 , respectively. These correspond to optical depths of 0.63 ± 0.14 and 0.50 ± 0.15 which are consistent within the error values. From the average of these two values, the optical depth of NH_3 (1,1) in AFGL 333-Ridge was derived to be 0.57 ± 0.10 .

The rotational temperature is determined from the the intensity ratio of (2,2) to (1,1) lines,

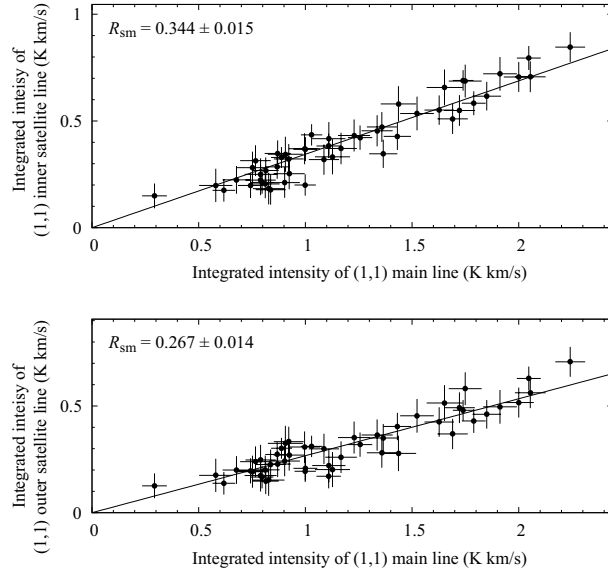


Fig. 7. Correlations of the integrated intensity in the (1,1) main and satellite lines. The correlations of the main to the inner and outer satellite lines are shown in the top and bottom panel, respectively. Data detected over the 2σ level in both the main and the satellite lines are plotted. The error bar shows the 1σ noise level. The estimated intensity ratio is shown in the top left corner of each panel.

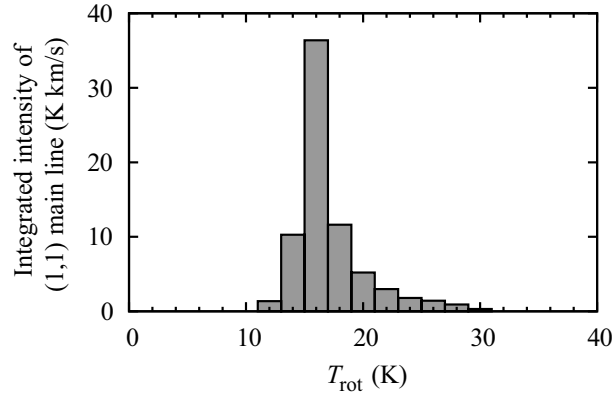


Fig. 8. Histograms of the rotational temperature. The integrated intensity of the (1,1) main line is each rotational temperature.

assuming that the (1,1) and (2,2) lines are emitted from the same gas. If the dynamical state and the excitation conditions are similar, the line shapes of (1,1) and (2,2) emission should be similar too. To check the similarity, we made gaussian fitting to the (1,1) and (2,2) lines. The obtained central velocity and the velocity width are $-48.67 \pm 0.03 \text{ km s}^{-1}$ and $1.92 \pm 0.06 \text{ km s}^{-1}$ for the (1,1) line, $-48.60 \pm 0.09 \text{ km s}^{-1}$ and $1.75 \pm 0.20 \text{ km s}^{-1}$ for the (2,2) line. They are consistent each other. In the case that the optical depth is uniform, the rotational temperature, T_{rot} , is directly derived from the the intensity ratio of the (2,2) to (1,1) line. Following Ho & Townes (1983), we derived the rotation temperature as:

$$T_{\text{rot}}(2, 2; 1, 1) = -41.5 \left/ \ln \left(\frac{-0.282}{\tau(1, 1, m)} \times \ln \left[1 - \frac{T_a(2, 2)}{T_a(1, 1)} \times \{1 - \exp[-\tau(1, 1, m)]\} \right] \right) \right. \quad (2)$$

The average intensity ratio is obtained to be 0.336 ± 0.020 from the correlation plot of the integrated intensity in the (1,1) main and (2,2) main lines. However the intensity ratio seems to change in the range from 0.2 to 1.0. This indicates the rotational temperature is different with the observed positions. Figure 8 shows a histogram of the rotational temperature for the (1,1) integrated intensity with 2σ detection in both the (1,1) and (2,2) lines. The (3,3) line was used to discuss the interstellar shock through the abundance of the ortho-to-para NH_3 . However, the average intensity ratio of (1,1) line to (3,3) line in this region is not high (0.20 ± 0.02) as a typical molecular clouds in the galactic disk (Nagayama et al. 2009), implying that the special condition as the interstellar shock is not necessarily required. The value of rotational temperature ranges between 12 – 30 K. The mean value and standard deviation of the rotational temperature were derived to be 17 K and 3 K, respectively. Scan positions that derived temperatures in the range of $T_{\text{rot}} = 12 - 22$ K and $23 - 30$ K account for 94% and 6% of the total integrated intensity, respectively. $T_{\text{rot}} = 12 - 22$ K is consistent with the dust temperature estimated from the Herschel data of AFGL 333-Ridge (Rivera-Ingraham et al. 2013). Figure 9 shows the rotational temperature map. The gas with a rotational temperature higher than the dust temperature (23 – 30 K) seem to be located at north, east, and south sides of the ridge. The temperature is enhanced nearly 10 K near the ionization front facing W4. Such an enhancement is also seen in the excitation temperature of CO (Sakai et al. 2006; Polychroni et al. 2012).

The column density of NH_3 can be estimated from the column density of (1,1) line and the rotational temperature using the assumption of Local Thermal Equilibrium (LTE) (Mangum et al. 1992).

$$N(1, 1) = 2.78 \times 10^{13} \tau(1, 1, m) \left(\frac{T_{\text{rot}}}{[\text{K}]} \right) \left(\frac{\Delta v_{1/2}}{[\text{km s}^{-1}]} \right) [\text{cm}^{-2}] \quad (3)$$

The column density of the (1,1) line can be estimated from the product of the optical depth of the (1,1) line, the rotational temperature, and the velocity width (FWHM) of the (1,1) line. We used a uniform optical depth of 0.57 ± 0.10 for the whole observed area. We used the rotational temperature and the velocity width obtained at each observed positions shown in figure 9 and 4.

Again, using the LTE assumption, the total column density of NH_3 which is sum of the column density of each rotational levels, was estimated using the column density of (1,1) line and the rotational temperature at each observed position. The column density map is shown in figure 9. The mean column density was obtained to be $(1.4 \pm 0.4) \times 10^{15} \text{ cm}^{-2}$. The error is the standard deviation

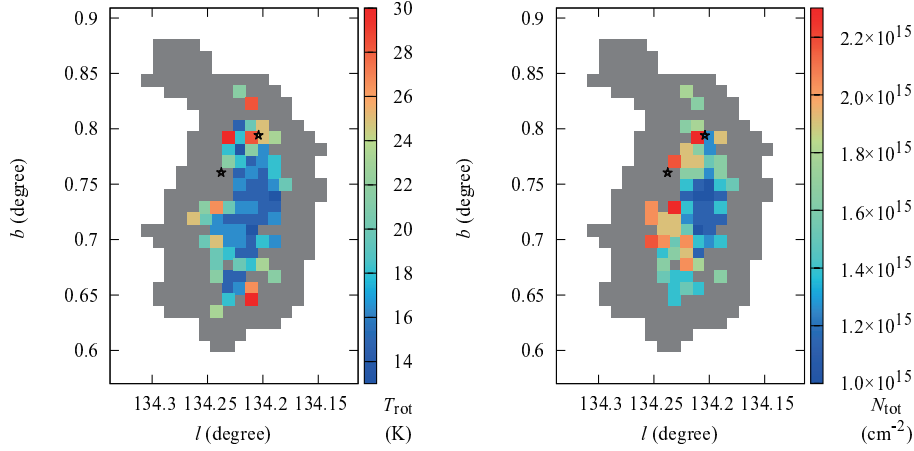


Fig. 9. Rotational temperature map (left) and column density map (right). Stars indicate the positions of two IRAS sources as figure 4.

of whole observed area.

The derived column density is compared with other observational results. Morgan et al. (2014) made ammonia observations by a petal-shaped scan centered on sub-mm sources in W3 GMC. Their six ammonia clumps, W48-W53, are located within our observed region excluding W54, which corresponds to SFO 05. The column densities of their sources, W48, W49, and W50, which are located near the AFGL 333-Ridge is $(5.1 \pm 0.5) \times 10^{14} \text{ cm}^{-2}$. However, for the sources in the eastern side of AFGL 333-Ridge (W51, W52, and W53), the column density is $(6.8 \pm 1.5) \times 10^{14} \text{ cm}^{-2}$. Although their values are nearly a third of ours ($10 - 19 \times 10^{14} \text{ cm}^{-2}$), the column density is higher at the eastern side of the AFGL 333-Ridge. Rivera-Ingraham et al. (2013) showed the H_2 column density map of AFGL 333 region by the Herschel HOBYS data. The central column density is $100 \times 10^{21} \text{ cm}^{-2}$. Figure 10 shows their contours of the H_2 column density overlaid on our NH_3 column density map. As the increase of the NH_3 column density is mainly around the positions of large velocity widths, one possible cause is the NH_3 velocity width. Another cause might be due to the actual NH_3 abundance or excitation conditions within the clumps (Morgan et al. 2014). If we adopt $N(\text{H}_2)$ derived from dust continuum (Rivera-Ingraham et al. 2013), the abundance ratio of NH_3 relative to H_2 , $X(\text{NH}_3)$, is 3×10^{-8} at the eastern edge and 1×10^{-8} at the central ridge.

The LTE mass of the cloud, M_{LTE} , was estimated from the sum of the LTE mass obtained at each observed grid, M_g , using $M_{\text{LTE}} = \sum M_g = \sum S_g N(\text{NH}_3)_g m(\text{H}_2) / X(\text{NH}_3)$, where S_g is the grid area of $37.5'' \times 37.5'' = 0.13 \text{ pc}^2$, $N(\text{NH}_3)_g$ is the column density of NH_3 at each observed grid shown in figure 9, $m(\text{H}_2)$ is the mass of the hydrogen molecule. The fractional abundance of NH_3 has typical values of 10^{-9} to 10^{-7} in dense gas clumps (e.g. Ungerechts et al. 1980; Ho & Townes 1983; Tieftrunk et al. 1998). By assuming $X(\text{NH}_3)$ of 3×10^{-8} as in the case of other massive star forming regions (e.g. Dunham et al. 2010a; Urquhart et al. 2015) and infrared dark clouds (Chira et al. 2013),

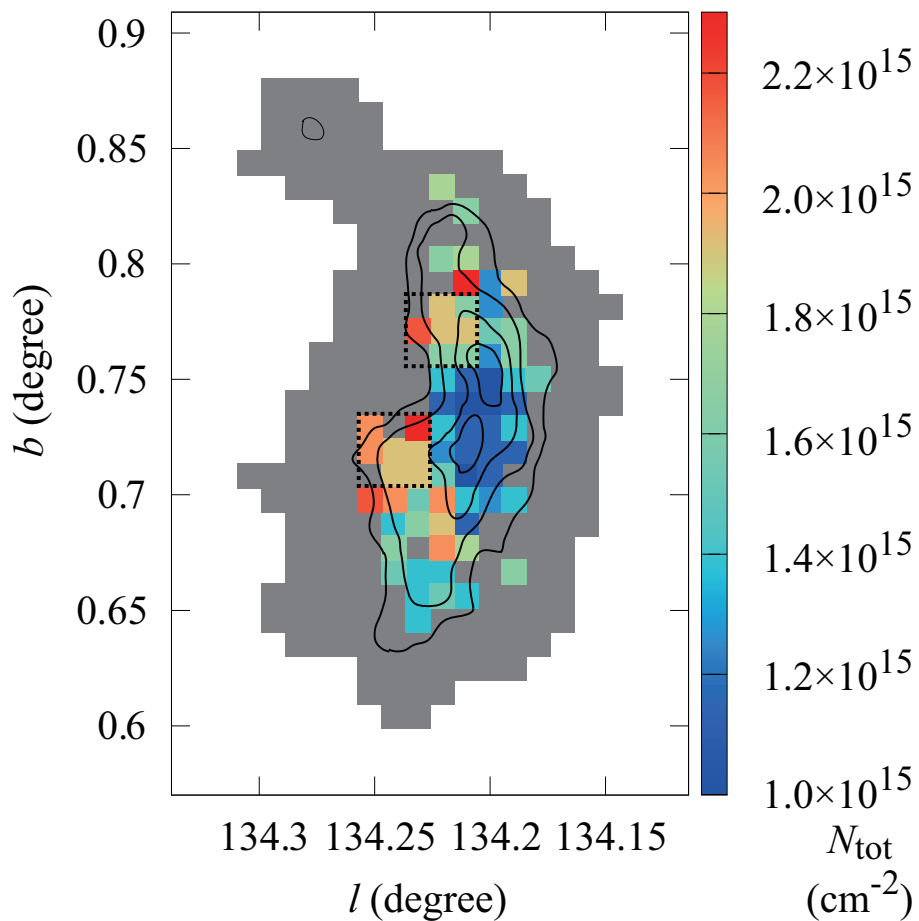


Fig. 10. H_2 column density contour (Rivera-Ingraham et al. 2013) overlaid on the NH_3 column density map.

the LTE mass of the cloud is $7700 \pm 1000 M_\odot$.

The other cloud mass estimation is the virial mass, M_{vir} . This is derived from $M_{\text{vir}} = 250R\Delta v^2$, where R is the radius of the cloud and Δv is the velocity width (Rohlfs & Wilson 1996). The virial mass within the radius of 1.6 pc ($0^\circ 10'$), which corresponds to the same area of the LTE mass estimation, was estimated to be $1800 \pm 400 M_\odot$. In this estimation, the mean velocity width of whole observed area of $2.15 \pm 0.46 \text{ km s}^{-1}$ was used. Our results suggest that the AFGL 333-Ridge is not close to a virialized state. Sakai et al. (2006) identified two cores, A and B, in the AFGL 333-Ridge from their C^{18}O observations. They derived the LTE masses and the virial masses of two cores, 2500 and 900 M_\odot , and 1400 and 500 M_\odot , for core A and B, respectively.

3.4 New H_2O Maser Detection

In star forming regions, H_2O masers serve as signposts of sites of active star formation. They may trace shocks, outflows, and other episodic events during the early formation stages of a protostar (Chibueze et al. 2012, 2014; Torrelles et al. 2011). Observing H_2O maser emission simultaneously to

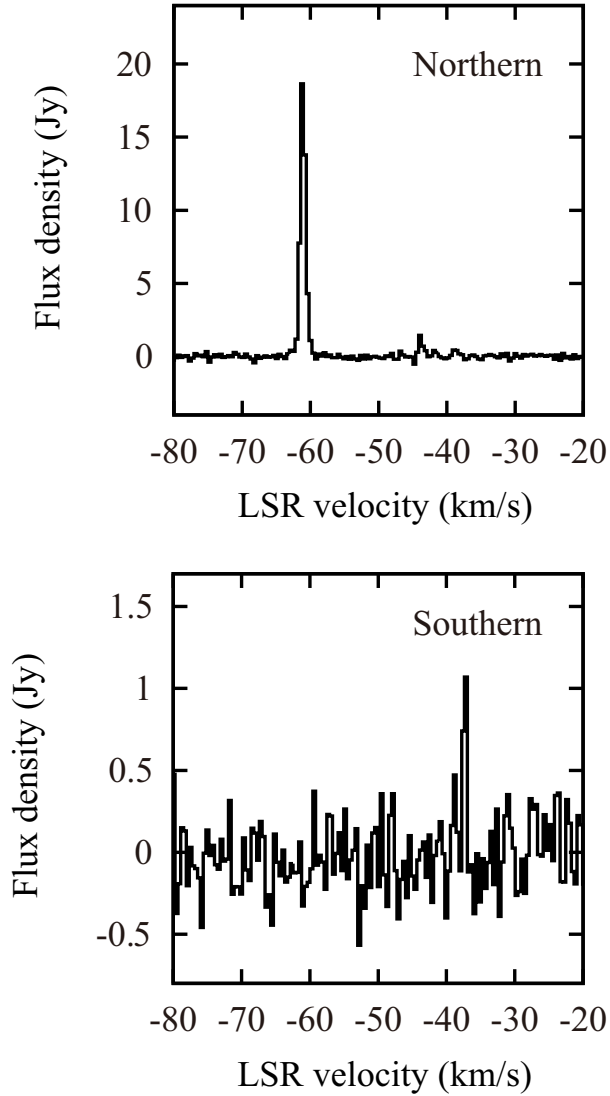


Fig. 11. H₂O maser spectra of the northern and the southern masers. Detected positions are listed in Table 1.

NH₃ lead us to detect H₂O masers at two different location in the region. For identification purposes, we will refer to these masers as the northern-maser and the southern-maser. The northern-maser is associated with SFO 05 and is a known maser which was reported by the maser survey of bright rimmed molecular clouds (Valdettaro et al. 2008). However, the position around the southern-maser was not searched before and not listed in any maser catalogs (e.g. Valdettaro et al. 2005; Sunada et al. 2007). The southern-maser is located near the center of AFGL 333-Ridge. Figure 11 shows the two H₂O maser spectra. The positions, radial velocities, and peak fluxes with uncertainty of the masers are shown in Table 1. The error in their determined positions is 30''.

We found a high velocity ¹²CO wing components, which suggest the activity of young stellar object. Figure 12 shows the distribution of the emission wings integrated over the velocity range -45

Table 1. H₂O Masers detected in our mapping observation.

Maser	l	b	α_{2000}	δ_{2000}	$v_{\text{LSR}}(\text{km s}^{-1})$	Peak flux (Jy)
Northern	134°2790	0°8571	02 ^h 29 ^m 02 ^s .0	+61°33'35"	-61 ± 0.4	18.44 ± 0.12
Southern	134°2069	0°7291	02 ^h 28 ^m 04 ^s .7	+61°28'01"	-36.9 ± 0.4	1.06 ± 0.14

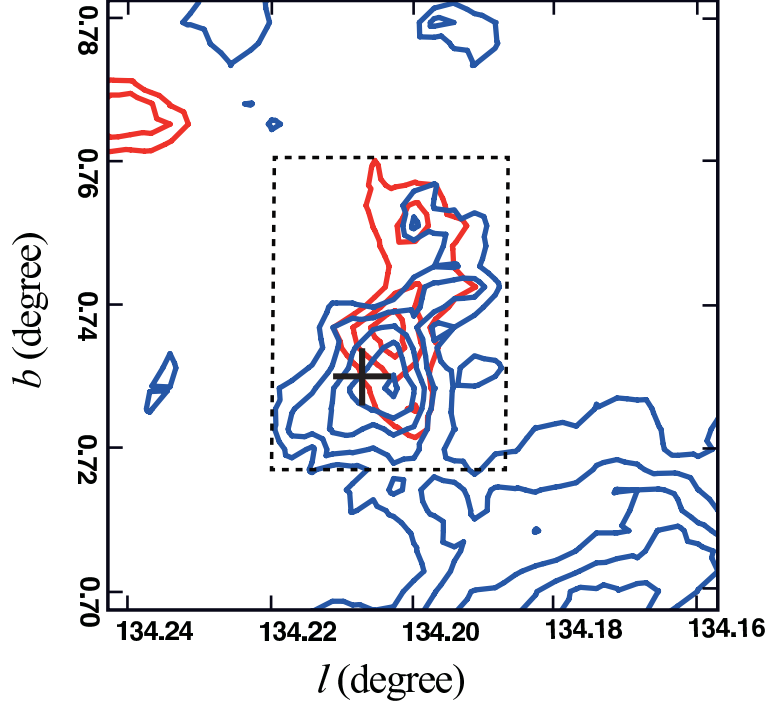


Fig. 12. Contour plot of ¹²CO J=2-1 red and blue outflow lobes. Velocities between -62.0 and -54.0 km s^{-1} are shown as blue contours and velocities between -43.0 and -35.0 km s^{-1} are shown in red contours. The blue component at the southwestern part is probably the contamination unrelated to the outflow associated with the young stellar activity. The lowest contour and contour interval are 3.4 K km s^{-1} (2σ) and 3.4 K km s^{-1} . A plus marks the location of the southern-maser. The dashed box shows the region where the physical parameters of the outflow are calculated.

Table 2. CO outflow parameters associated the southern H₂O maser.

Lobe	$M [M_{\odot}]$	$P [M_{\odot} \text{ km s}^{-1}]$	$E [M_{\odot} \text{ km}^2 \text{ s}^{-2}]$
Blue	0.76	4.97	32.4
Red	0.49	3.02	17.3

Table 3. YSO candidates near the southern H₂O maser, taken from Table 3 of Jose et al. (2016).

ID	α_{2000} (deg)	δ_{2000} (deg)	l (deg)	b (deg)	[3.6] (mag)	[4.5] (mag)	[5.8] (mag)	[8.0] (mag)	[24] (mag)	YSO Classification
1	37.0250	+61.4701	134.2082	0.7329	12.83	10.42	8.97	7.89	3.04	Class I
2	37.0258	+61.4689	134.2090	0.7319	12.83	11.18	10.02	9.20	...	Class I
3	37.0227	+61.4686	134.2077	0.7311	12.26	10.61	9.39	8.54	2.59	Class I
4	37.0159	+61.4634	134.2066	0.7251	14.96	13.96	12.82	11.98	...	Class I
5	37.0243	+61.4644	134.2100	0.7275	14.46	13.40	13.15	11.37	...	Class II

km s⁻¹ < v_{LSR} < -37 km s⁻¹ (red component), and -60 km s⁻¹ < v_{LSR} < -52.5 km s⁻¹ (blue component) around the southern-maser. The blue components at the southwestern part of the map is probably another velocity (-53 km s⁻¹) component. Our result suggests the bipolar molecular outflow is associated with the southern-maser. Assuming ¹²CO J=2-1 line is optically thin, and CO abundance relative to H₂ is 10⁻⁴, the lower limit of the outflow masses in the blue and red lobes. We restricted the area of the outflow within the box area of 150'' in latitude and 120'' in longitude, shown in the dashed box in figure 12. As the temperature of the warm gas in the outflow is uncertain, we choose $T_{\text{ex}} = 17.6$ K to minimize the column density as Dunham et al. (2010b). The calculated total mass, momentum and energy of the outflow in each lobe are shown in Table 2. There are four Class I and one Class II sources (Jose et al. 2016) within the positional accuracy of the southern-maser (table 3). All five sources were detected by the Spitzer IRAC bands, but have no NIR data, and two sources were detected by MIPS 24 μm band. It suggests that the outflow is powered by the source(s) among them.

4 Discussion

4.1 Star Formation Activity in the Region

There have been extensive studies on W3 GMC, but mainly on the most active star forming regions such as W3 Main and W3(OH). For example, the deep NIR imaging of the W3 Main, Bik et al. (2014) revealed the disk fraction of the young stellar content. The age of IC 1795 OB association was estimated to be 3-5 Myr by Oey et al. (2005) and Roccatagliata et al. (2011). Román-Zúñiga et al. (2015) identified five principal clusters and discussed the history of star formation in W3 Main and W3(OH). Across the W3 region, extensive survey of the high-mass stellar population by Kiminki et al. (2015) showed star formation in W3 began spontaneously up to 8–10 Myr ago. Rivera-Ingraham et al. (2015) made dust column density maps by using Herschel datasets in the whole

W3 complex, and created the probability density functions (PDFs). They analyzed PDF to show the stellar feedback-based constructive process, i.e. stellar feedback is a major player in the cluster formation and the overall characteristics and local evolution of GMC. They proposed a “convergent constructive feedback” model. They suggested the combined collection effect in compressing and confining material by the high mass stars create higher column densities by feedback, which lead to the creation of an environment suitable for high mass cluster formation.

Recently, Jose et al. (2016) made deep JHKs photometry of the AFGL 333 region, complementing with Spitzer IRAC and MIPS observations. Their new NIR photometry is > 3 mag deeper in each band compared to the 2MASS photometry, and they identified many YSOs including low mass populations in this region. To explore the distribution of YSOs in our observational field, we used their candidate sources of Class I and II. Figure 13a shows the plot of distribution of the YSOs. As their field is not fully covered our mapping area of NH_3 observations, we supplemented by the Spitzer YSO catalog (Catalog 1) of Rivera-Ingraham et al. (2011). That is why the surface density of Class II sources in the southern region appears to be low. A rich clustering of Class 0/I objects is seen along AFGL 333-Ridge and in the core region, where the southern-maser source and NH_3 peak lie. Although in the Spitzer Catalog 1 clusterings are not found around the positions of two IRAS sources because of confusion by the bright infrared nebulosities, the deep NIR observations by Jose et al. (2016) clearly revealed some peaks of the YSO surface density associated with AFGL 333-Ridge and its surroundings. The peak around IRAS 02245+6115 was already discussed by Carpenter et al. (2000). Bica et al. (2003) also listed it with the size of $1'.7 \times 1'.5$ in the catalog of infrared clusters and stellar groups. IRAS 02245+6115 is associated with compact HII region G 134.2+0.8 (Hughes & Viner 1982) which has an electron density of 450 cm^{-3} and size of 0.3 pc. The peak of the 5 GHz continuum emission agrees well with IRAS 02245+6115 within a positional uncertainty of $27'' \times 9''$ in position angle 58° (see figure 13b). One of the Class I source at $(l, b) = (134.^\circ 2344, 0.7497)$, which also corresponds to this peak, have $J = 15.98$, $H = 13.34$, and $K_s = 11.71$ (Jose et al. 2016). The extinction map made from the CO column density (Jose et al. 2016) indicates $A_v \sim 25$ mag around G 134.2+0.8. On the NIR color-magnitude diagram (figure 8 by Jose et al. (2016)), its location is consistent with deeply embedded star with the mass of more than $10 M_\odot$ using the 2 Myr isochrone by Bressan et al. (2012). Thus, this source should be the exciting star of the compact HII region as suggested by Mampaso et al. (1984). Most YSOs are distributed in the south-western of this peak of radio continuum emission. Another IRAS source, IRAS 02244+6117, is a bright infrared source BIRS-104 (Elmegreen et al. 1980) and a small arc of infrared emission around it is reported by Kraemer et al. (2003). The peak of YSO surface distribution at the south of IRAS 02244+6117 is also evident. As the northern part of AFGL 333-Ridge is located between these two IRAS sources, Rivera-Ingraham

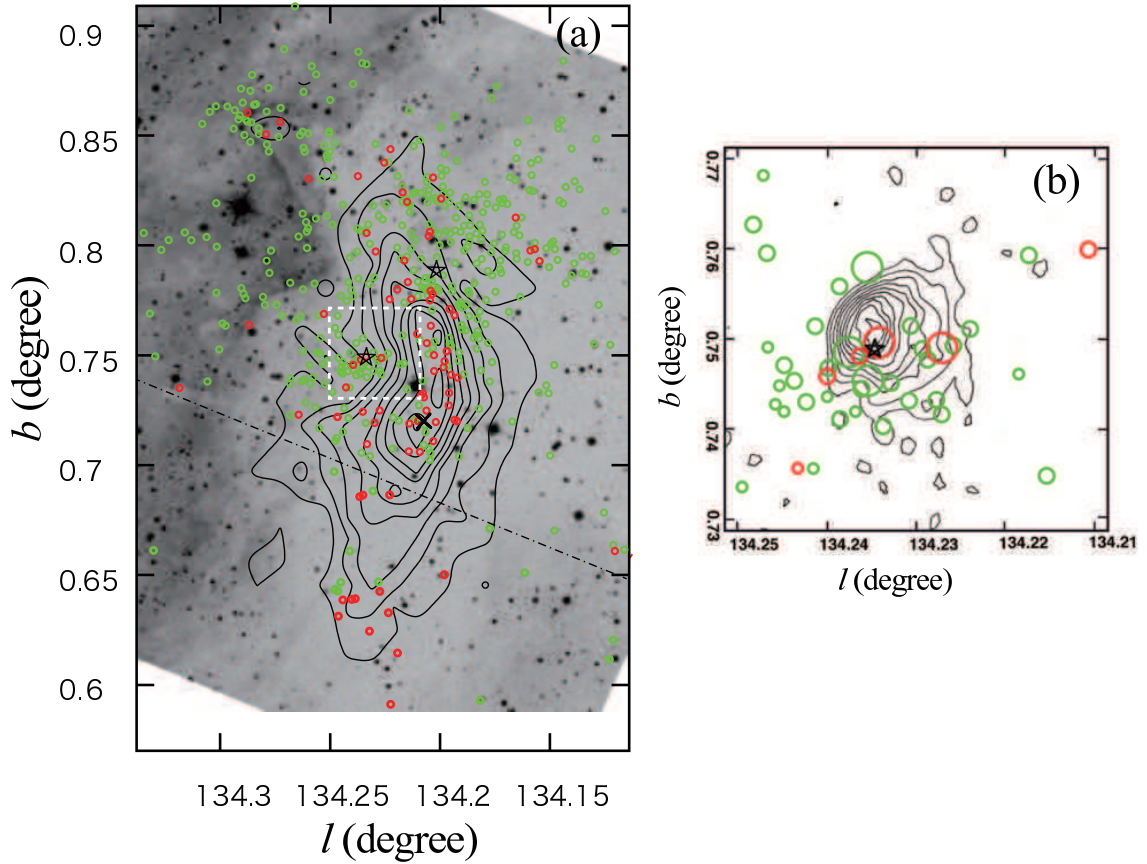


Fig. 13. (a) Distribution of YSOs and the contour map of NH_3 integrated intensity overlaid on the DSS-R image. Class I, Class II sources (Jose et al. 2016) are shown in red and green circles, respectively. In the southern part below the dash-dotted line, Class 0/I and Class II sources by Rivera-Ingraham et al. (2011) are shown. Two IRAS sources and an NH_3 peak position are shown in stars and x, respectively. (b) YSOs with NIR color data in the box of $0''.04$ around IRAS02245+6115, which is shown with white dashed line in (a), are overlaid on the synthesis radio continuum map (Hughes & Viner 1982). YSOs are shown by the symbols in different size according to their mass estimated based on the color magnitude ($J - H$ vs J) diagram by Jose et al. (2016). Sources with $M < 1.0M_\odot$, $M = 1.0 - 10.0M_\odot$, and $M > 10M_\odot$ are shown in small, medium, and large circles, respectively.

et al. (2011) suggested the star formation activity of AFGL 333-Ridge has been induced by these two sources. The substructure of AFGL 333-Ridge could be affected by the feedback from the young stellar activities.

SFO 05 at the northern end of AFGL 333-Ridge is the typical case of star formation triggered by radiation-driven implosion. A pre-existing condensation of about $400M_{\odot}$ was compressed by the pressure of the ionizing radiation of W4 (Fukuda et al. 2013). And the compact HII region G 134.2+0.8 lies at the interface between the AFGL 333-Ridge and W4. This implies that the B0.5 star exciting the HII region G 134.2+0.8 (Hughes & Viner 1982) could have been formed due to the influence of the expanding bubble of W4. The large-scale temperature enhancement in the eastern side of the AFGL 333-Ridge suggests an interaction between the dense ridge and the W4 bubble. The interaction with the compact HII region may be limited to only the periphery or the north-south direction where large velocity widths were observed. The low ionizing flux can erode the cloud, but would not trigger the formation of stars (Bisbas et al. 2011). Previous studies (e.g. Oey et al. 2005; Lefloch et al. 1997) support a triggered or induced mode of star formation to be responsible for the formation of the stars at the interface between the W4 and the dense cloud, AFGL 333-Ridge. We suggest the overall structure of AFGL 333-Ridge has been made by the external feedback from W4. Although the local stellar feedback was also acting to make small-scale structure of the cloud, the convergent constructive process (Rivera-Ingraham et al. 2013) did not work effectively in this region.

Quiescent mode of star formation can be described as a mode of star formation with minimal external influence. Based on the evidence seen in small velocity widths in the NH_3 lines around this region, the younger generation of YSOs distributed around the center of the peak of the NH_3 (1,1) emission at the core of AFGL 333-Ridge may have formed spontaneously. Dale et al. (2015) gave a warning in distinguishing triggered population from spontaneously formed ones, and interpreting the observational data of star forming region in terms of triggering. Although our observations show G 134.2+0.8 and the W4 bubble are interacting with AFGL 333-Ridge and has affected its structure, it is not evident that most stars in this region were formed by the induced mode. Jose et al. (2016) compared the star formation efficiency and rate with W3 Main and the nearby low-mass star forming regions, and showed the star forming activity in AFGL 333 region is comparable to other low-mass regions. As the mass of the cloud estimated by them is consistent with ours, the star formation efficiency ($\text{SFE} = M_{\text{star}} / (M_{\text{star}} + M_{\text{cloud}})$) is as low as 3%. The stellar feedback has not globally enhanced the star forming activity in this region. Our finding of the small velocity width of NH_3 line in the AFGL 333-Ridge and the existing literatures as an older population in the western side of the AFGL 333 region suggest apparent coexistence of induced and quiescent modes of star formation within several parsec scale.

4.2 Interaction Between compact HII Region G 134.2+0.8 and Dense Molecular Cloud

NH_3 clumps associated with active star forming regions exhibit large emission line velocity widths driven by inflow or outflow within the gas, other non-thermal turbulent motion, or numerous unresolved dense clumps (e.g. Hindson et al. 2010; Urquhart et al. 2011). In the case of Gem OB1 cloud, the dense cloud in contact with an expanding HII region showed no obvious observable interaction between them (Chibueze et al. 2013). On the other hand, the observed large velocity widths found in the northern and southern surroundings of HII region G 134.2+0.8 (see figure 4) is evident, and these feature suggests G 134.2+0.8 is interacting with the dense molecular gas of AFGL 333-Ridge. No NH_3 emission was detected in and to the east of G 134.2+0.8, but the NH_3 emission detected to the west of it (around the center of AFGL 333-Ridge) showed no significant velocity width. The surface of the cloud might be irradiated by UV photons from the G 134.2+0.8. Based on the Lyman continuum photon number from B0.5 exciting star of HII region G 134.2+0.8 at 1 pc from AFGL 333-Ridge is $8 \times 10^8 \text{ cm}^{-2}\text{s}^{-1}$. Even at the distance of 16–20 pc from seven exciting stars of W4 (Lefloch et al. 1997), the ionizing flux is $4 \times 10^9 \text{ cm}^{-2}\text{s}^{-1}$ at AFGL 333-Ridge. These photon flux is approximately one order of magnitude smaller than for the typical star forming clouds at the edge of HII bubbles described in the collect-and-collapse model (e.g. Deharveng et al. 2003). The activity of young stars embedded in the cloud might be a source of turbulent motion, but there is not so many young objects in these regions. One explanation for the north-south alignment of this interaction could be an injection of mechanical energy from YSO jets or high-velocity outflows located near the center of G 134.2+0.8, interacting with the dense cloud around it. Although, such shock activities provide possible explanation for the observed large velocity widths, CO observations by Sakai et al. (2006) show no sign of a high velocity component expected in the case of such outflows. The systematic outflow survey of IRAS sources by Snell et al. (1990) also reported negative results for the AFGL 333 region. However, we should notice that CO observations by Sakai et al. (2006) were not so deep to detect faint high velocity wing, because their work was to study the physical and chemical states of the cloud. And the central mapping position by Snell et al. (1990) was different from IRAS 02245+6115.

Figure 14 shows two large velocity width regions of NH_3 emission on the contours of 1420 MHz radio continuum (Taylor et al. 2003) and the integrated ^{13}CO J=2-1 intensity map. The radio continuum emission of G 134.2+0.8 fits into the hole of the ^{13}CO map. The cavity or shell-like structure of ^{13}CO emission with the size of $2'$ (1.2 pc) hosting the dense ionized gas is reminiscent of the molecular dissociation or dynamical effect of the HII region on the molecular cloud. There is the submillimeter source ID-298 (Moore et al. 2007) at the eastern side of the compact HII region, which corresponds to the CO clump. The synthesized radio continuum map of G 134.2+0.8 (Hughes

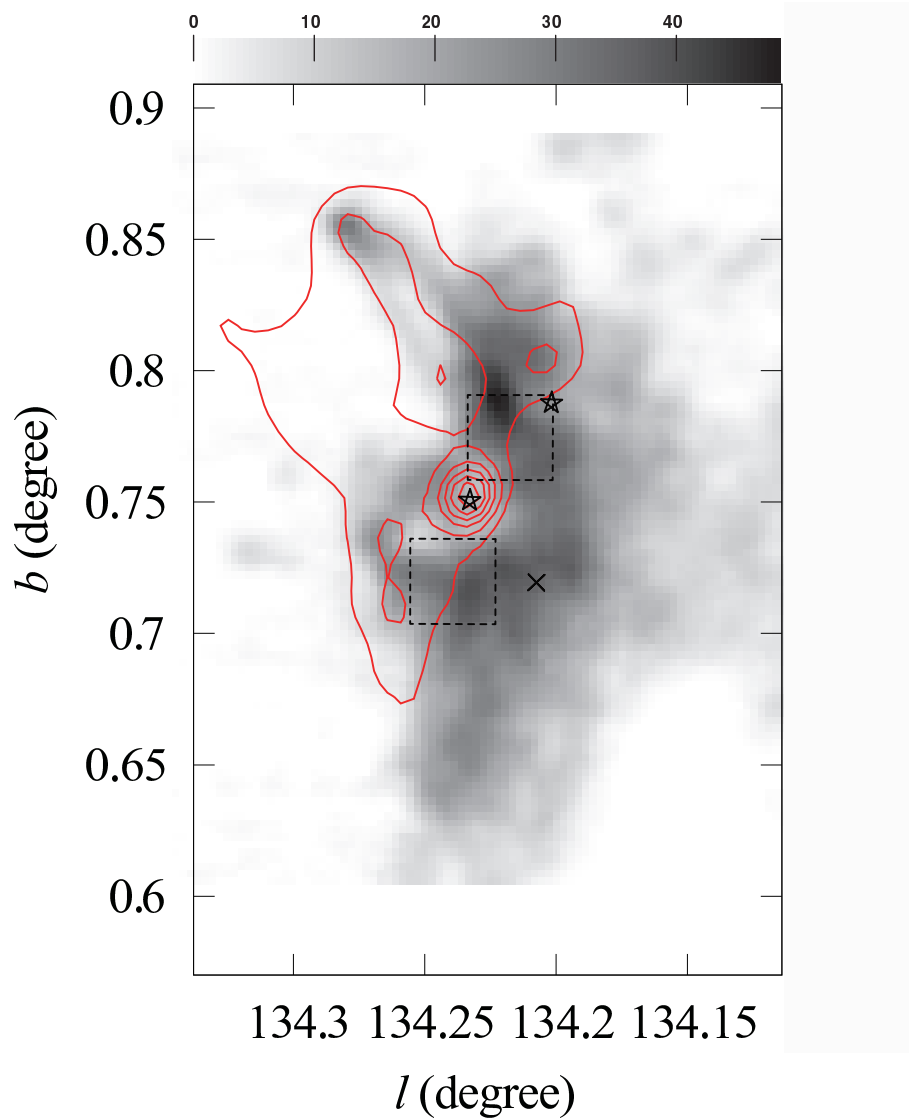


Fig. 14. The regions of large NH_3 velocity width are shown in the dashed boxes on the red contours of the 1420 MHz radio continuum emission (Canadian Galactic Plane Survey; Taylor et al. (2003)), with contours incremented in 2 K intervals beginning with 18 K in brightness temperature, and the gray-scale map of integrated ^{13}CO J=2-1 emission. Two IRAS sources and an NH_3 peak position are shown in stars and x, respectively.

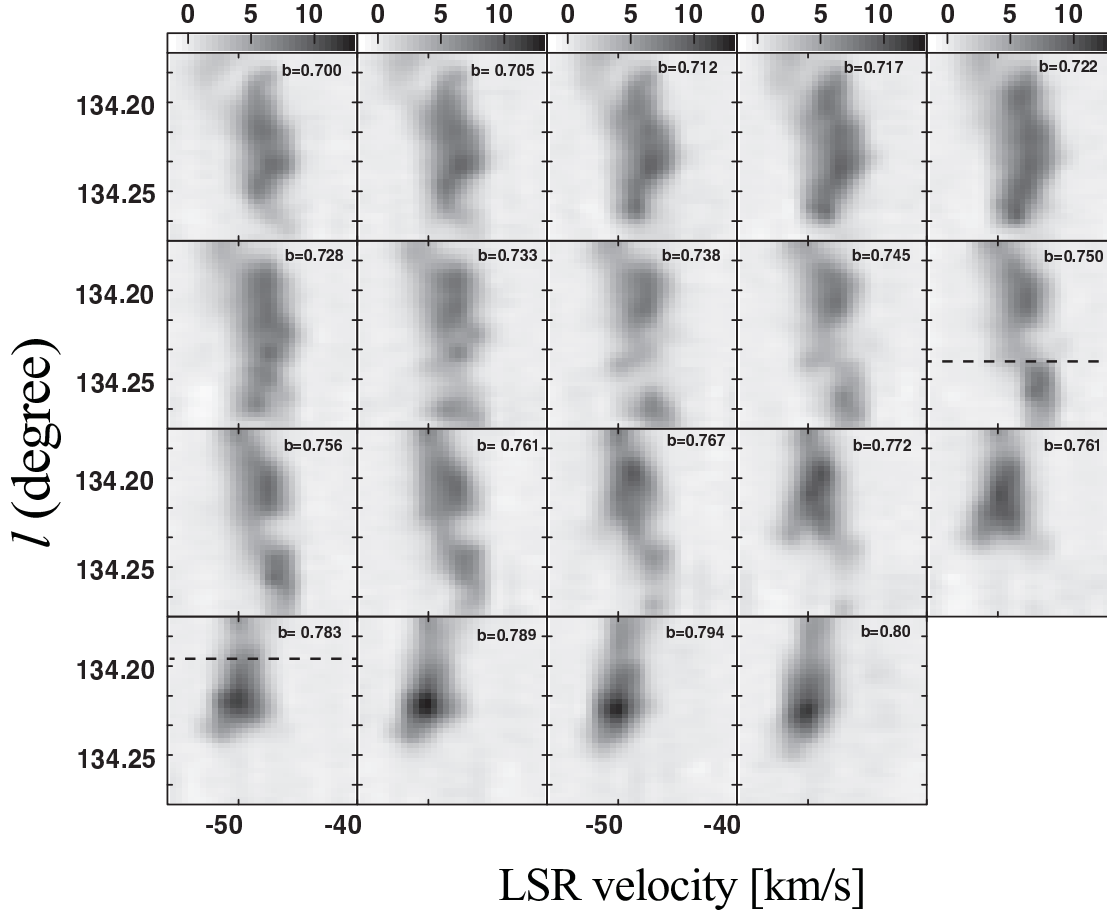


Fig. 15. Position-velocity diagrams of ^{13}CO J=2-1 line. The positions of IRAS 02245+6115 and IRAS 02244+6117 are shown in the dashed lines.

& Viner 1982) shows steep decline of intensity toward the eastern direction (see figure 13b). This asymmetric structure of radio continuum map suggests that a B0.5 star has been formed near this CO clump, and the compact HII region is expanding to the western direction.

Figure 15 shows the position-velocity diagrams of ^{13}CO J=2-1 emission along the galactic longitude. The positions of IRAS 02245+6115 and IRAS 02244+6117 are shown by the dashed lines in the panel of $b = 0.750$ and $b = 0.783$, respectively. From $b = 0.750$ to $b = 0.761$, we can trace the C-shaped velocity structure (blue shifted to $\sim -49 \text{ km s}^{-1}$) centered around $l = 134.23$. Such a structure also shows the evidence of the shell with the expanding motion of $\sim 2 \text{ km s}^{-1}$. Contrary to the north and south of G 134.2+0.8, the reason for the NH_3 velocity width of 1.8 km s^{-1} at the west, nearly as low as the main part of the cloud, might be the geometrical effect. The most dense part of the NH_3 ridge is deeply embedded in AFGL 333-Ridge along the line of sight. G 134.2+0.8 is mostly

expanding into the west at the foreground of the NH_3 ridge, and could not interact in the western boundary of the compact HII region. The interaction is limited in the northern and the southern less dense part of the NH_3 ridge. The large velocity width around $(l, b) = (134.^\circ24, 0.^\circ761)$ in figure 15 corresponds to the northern large width NH_3 region.

Although SED of the exciting star candidate (see subsection 4.2) suggests that it is Class I source (Jose et al. 2016), there is no other characteristic signatures of young activity. Furthermore, because of its relatively low density, G 134.2+0.8 is not as young (Thronson et al. 1979) as the other compact or ultracompact HII regions, like G 133.8+1.4 (W3 N) and W3 (OH) (Carpenter et al. 2000), associated with infrared sources in the W3/W4 region. For the large line width regions of NH_3 emission, the explanation invoking interaction by the expanding motion of the ionized gas at the periphery of AFGL 333-Ridge is more preferable at present. The large line width could be due to turbulent motion supplied through the shock front of G 134.2+0.8 in the low ambient density. Molecular line observations with higher resolution is needed to clarify the activity of the YSOs in G 134.2+0.8.

5 Conclusions and Summary

Through our NH_3 mapping observations of AFGL 333 in the W4 region using the Nobeyama 45m radio telescope and archival CO and other data, we have explored the physical properties of this region and studied YSOs in two IRAS sources. Our results and conclusions are summarized as follows:

1. We derived a size of 2.0×0.6 pc, the rotational temperature of 12 – 30 K, and LTE mass of $7700 \pm 1000 M_\odot$ for the AFGL 333-Ridge molecular cloud. The viral mass was estimated to be $1800 \pm 400 M_\odot$. Possibly indicating that the AFGL 333-Ridge is not close to a virialized state. We found two regions of large NH_3 line width at the eastern side of AFGL 333-Ridge.

2. The large NH_3 line width at the north and the south of IRAS 02245+6115 suggests an interaction by the expanding motion of the ionized gas from the compact HII region G 134.2+0.8 at the periphery of AFGL 333-Ridge. ^{13}CO data obtained by HHT and NRO reveal a cavity structure with the size of 1.2 pc in the integrated intensity maps, with an expanding motion of a few km s^{-1} in the position velocity maps. However, the small velocity widths in NH_3 gas observed west of IRAS 02245+6115, around the center of the dense molecular gas, suggest that interaction with the compact HII region is limited.

3. Two H_2O masers were detected. The southern-maser at the core of AFGL 333-Ridge was a new finding. A CO bipolar outflow, a signpost of active star formation, was found near this maser source and it appears to be associated with some Class I/II sources.

4. We examined the distribution of YSOs in the AFGL 333 region, especially around

IRAS 02245+6115 and IRAS 02244+6117. We confirmed that G 134.2+0.8 associated with IRAS 02245+6115 is excited by a deeply embedded young intermediate-mass star. Although the W4 bubble and AFGL 333-Ridge have previously interacted, and induced mode of star formation could be responsible for the formation of SFO 05 and IRAS 02245+6115, the small velocity width, low rotational temperature of NH₃ line, and low SFE suggests that most stars in this region were formed by the quiescent mode in the feedback-driven structure. Depending on the local environment, both of the two modes of star formation, induced and quiescent, coexist in scales of several pc or less. It appears that star formation in this region has taken place mainly without an external trigger, but accompanying stellar feedback environment.

Acknowledgments

We are grateful to the staff members of the Nobeyama Radio Observatory (NRO) for observation support. We also thank John Bieging for providing Heinrich Hertz Telescope CO data cubes and Takeshi Sakai for providing his NRO maps of the CO emission in FITS format. The research presented in this paper has used data from the Spitzer Space Telescope, which is operated by the Jet Propulsion Laboratory, California Institute of Technology, under contract with NASA, and the Canadian Galactic Plane Survey supported by the Natural Sciences and Engineering Research Council.

References

- Ballantyne, D. R., Kerton, C. R., & Martin, P. G. 2000, *ApJ*, 539, 283
- Bica, E., Dutra, C. M., & Barbuy, B. 2003, *A&A*, 397, 177
- Bieging, J. H., & Peters, W. L. 2011, *ApJS*, 196, 18
- Bik, A., Stolte, A., Gennaro, M. et al. 2014, *A&A*, 561, A12
- Bisbas, T. G., Wünsch, R., Whitworth, A. P. et al. 2011, *ApJ*, 736, 142
- Bressan, A., Marigo, P., Girardi, L. et al. 2012, *MNRAS*, 427, 127
- Carpenter, J. M., Heyer, M. H., & Snell, R. L. 2000, *ApJS*, 130, 381
- Chibueze, J. O., Imai, H., Tafuya, D. et al. 2012, *ApJ*, 748, 146
- Chibueze, J. O., Imura, K., Omodaka, T. et al. 2013, *ApJ*, 762, 17
- Chibueze, J. O., Omodaka, T., Handa, T. et al. 2014, *ApJ*, 784, 114
- Chira, R. -A., Beuther, H., Linz, H. et al. 2013, *A&A*, 552, A40
- Dale, J. E., Haworth, T. J., & Bressert, E. 2015, *MNRAS*, 450, 1199
- Deharveng, L., Lefloch, B., Zavagno, A. et al. 2003, *A&A*, 408, L25
- Deharveng, L., Zavagno, A., & Caplan, J. 2005, *A&A*, 433, 565
- Di Francesco, J., Johnstone, D., Kirk, H. et al. 2008, *ApJS*, 175, 277
- Dunham, M. K., Rosolowsky, E., Evans, N. J. II et al. 2010a, *ApJ*, 717, 1157
- Dunham, M. K., Evans, N. J. II, Bourke, T. L. et al. 2010b, *ApJ*, 721, 995

Elmegreen, D. M. 1980, *ApJ*, 240, 846

Elmegreen, B. G., & Lada, C. J. 1977, *ApJ*, 214, 725

Feigelson, E. D., & Townsley, L. K. 2008, *ApJ*, 673, 354

Fukuda, N., Miao, J., Sugitani, K., et al. 2013, *ApJ*, 773, 132

Hachisuka, K., Brunthaler, A., Menten, K. M. et al. 2006, *ApJ*, 645, 337

Hindson, L., Thompson, M. A., Urquhart, J. S. et al. 2010, *MNRAS*, 408, 1438

Ho, P. T. P., & Townes, C. H. 1983, *ARA&A*, 21, 239

Hughes, V. A., & Viner, M. R. 1982, *AJ*, 87, 685

Jose, J., Kim, S. K., Herczeg, G. J. et al. 2016, *ApJ*, 822, 49

Kiminki, M. M., Kim, J. S., Bagley, M. B. et al. 2015, *ApJ*, 813, 42

Kraemer, K. E., Shipman, R. F., Price, S. D. et al. 2003, *AJ*, 126, 1423

Kutner, M. L., & Ulich, B. L. 1981, *ApJ*, 250, 341

Lada, C. J., Elmegreen, B. G., Cong, H.-I., & Thaddeus, P. 1978, *ApJL*, 226, L39

Lefloch, B., Lazareff, B., & Castets, A. 1997, *A&A*, 324, 249

Lefloch, B., & Cernicharo, J. 2000, *ApJ*, 545, 340

Mampaso, A., Gomez, P., Sanchez-Magro, C. & Selby, M. J. 1984, *MNRAS*, 207, 465

Mangum, J. G., Wootten, A., & Mundy, L. G. 1992, *ApJ*, 388, 467

Moore, T. J. T., Bretherton, D. E., Fujiyoshi, T. et al. 2007, *MNRAS*, 379, 663

Morgan, L. K., Figura, C. C., Urquhart, J. S. & Thompson, M. A. 2010, *MNRAS*, 408, 157

Morgan, L. K., Moore, T. J. T., Eden, D. J. et al. 2014, *MNRAS*, 440, 1730

Nagayama, T., Omodaka, T., Handa, T. et al. 2009, *PASJ*, 61, 1023

Oey, M. S., Watson, A. M., Kern, K., & Walth, G. L. 2005, *AJ*, 129, 393

Polychroni, D., Moore, T. J. T., & Allsopp, J. 2012, *MNRAS*, 422, 2992

Rivera-Ingraham, A., Martin, P. G., Polychroni, D., & Moore, T. J. T. 2011, *ApJ*, 743, 39

Rivera-Ingraham, A., Martin, P. G., Polychroni, D. et al. 2013, *ApJ*, 766, 85

Rivera-Ingraham, A., Martin, P. G., Polychroni, D. et al. 2015, *ApJ*, 809, 81

Roccatagliata, V., Bouwman, J., Henning, T., et al. 2011, *ApJ*, 733, 113

Rohlfs, K., & Wilson, T. L. 1996, *Tools of Radio Astronomy* (2nd edition; Berlin: Springer)

Román-Zúñiga, C. G., Ybarra, J. E., Megías, G. D. et al. 2015, *AJ*, 150, 80

Sakai, T., Oka, T., & Yamamoto, S. 2006, *ApJ*, 649, 268

Sakai, T., Oka, T., & Yamamoto, S. 2007, *ApJ*, 662, 1043

Snell, R. L., Dickman, R. L., & Huang, Y.-L. 1990, *ApJ*, 352, 139

Sugitani, K., Fukui, Y., & Ogura, K. 1991, *ApJS*, 77, 59

Sunada, K., Nakazato, T., Ikeda, N. et al. 2007, *PASJ*, 59, 1185

Taylor, A. R., Gibson, S. J., Peracaula, M. et al. 2003, AJ, 125, 3145
Tieftrunk, A. R., Megeath, S. T., Wilson, T. L., & Rainer, J. T. 1998, A&A, 336, 991
Thronson, H. A., Harvey, P. M., & Gatley, I. 1979, ApJ, 229, L133
Thronson, H. A., Lada, C. J., & Hewagama, T. 1985, ApJ, 297, 662
Torrelles, J. M., Patel, N. A., Curiel, S. et al. 2011, MNRAS, 410, 627
Ungerechts, H., Walmsley, C. M., & Winnewisser, G. 1980, A&A, 88, 259
Urquhart, J. S., Morgan, L. K., Figura, C. C. et al. 2011, MNRAS, 418, 1689
Urquhart, J. S., Figura, C. C., Moore, T. J. T. et al. 2015, MNRAS, 452, 4029
Valdettaro, R., Palla, F., Brand, J., & Cesaroni, R. 2005, A&A, 443, 535
Valdettaro, R., Migenes, V., Trinidad, M. A., Brand, J., & Palla, F. 2008, ApJ, 675, 1352
Whitworth, A. P., Bhattal, A. S., Chapman, S. J. et al. 1994, MNRAS, 268, 291
Xu, Y., Reid, M. J., Zheng, X. W., & Menten, K. M. 2006, Science, 311, 54